European Journal of Mechanics B/Fluids 28 (2009) 728–743

Contents lists available at ScienceDirect

European Journal of Mechanics B/Fluids

journal homepage: www.elsevier.com/locate/ejmflu

Computational and experimental investigation of flow over a transient pitching hydrofoil

Antoine Ducoin [a,*], Jacques André Astolfi [a], François Deniset [a], Jean-François Sigrist [b]

[a] Institut de Recherche de l'Ecole Navale EA 3634, Ecole Navale, 29240 Brest Armées, France
[b] DCNS Propulsion, 44620 La Montagne, France

ARTICLE INFO

Article history:
Received 28 October 2008
Received in revised form
15 April 2009
Accepted 3 June 2009
Available online 12 June 2009

Keywords:
Lifting bodies
Hydrodynamic loading
Transient regimes
Laminar to turbulent transition

ABSTRACT

The present study is developed within the framework of marine structure design operating in transient regimes. It deals with an experimental and numerical investigation of the time–space distribution of the wall-pressure field on a NACA66 hydrofoil undergoing a transient up-and-down pitching motion from 0° to 15° at four pitching velocities and a Reynolds number $Re = 0.75 \times 10^6$. The experimental investigation is performed using an array of wall-pressure transducers located on the suction side and by means of time–frequency analysis and Empirical Modal Decomposition method. The numerical study is conducted for the same flow conditions. It is based on a 2D RANS code including mesh reconstruction and an ALE formulation in order to take into account the foil rotation and the tunnel walls. Due to the moderate Reynolds number, a laminar to turbulent transition model was also activated. For the operating flow conditions of the study, experimental and numerical flow analysis revealed that the flow experiences complex boundary layer events as leading-edge laminar separation bubble, laminar to turbulent transition, trailing-edge separation and flow detachment at stall. Although the flow is relatively complex, the calculated wall pressure shows a quite good agreement with the experiment provided that the mesh resolution and the temporal discretization are carefully selected depending on the pitching velocity. It is particularly shown that the general trend of the wall pressure (low frequency) is rather well predicted for the four pitching velocities with for instance a net inflection of the wall pressure when transition occurs. The inflection zone is reduced as the pitching velocity increases and tends to disappear for the highest pitching velocity. Conversely, high frequency wall-pressure fluctuations observed experimentally are not captured by the RANS model. Based on the good agreement with experiment, the model is then used to investigate the effects of the pitching velocity on boundary layer events and on hydrodynamic loadings. It is shown that increasing the pitching velocity tends to delay the laminar-to-turbulence transition and even to suppress it for the highest pitching velocity during the pitch-up motion. It induces also an increase of the stall angle (compared to quasi-static one) and an increase of the hysteresis effect during pitch-down motion resulting to a significant increase of the hydrodynamic loading.

1. Introduction

The prediction of the forces acting on lifting bodies operating in forced motions of large amplitude is fundamental for design and sizing of marine structures such as rudders, stabilizers, marine propeller blades but also for innovative and complex propulsion systems based on like-fish propulsion [1]. Basically, it requires the knowledge of unsteady boundary layer in forced motions including the understanding of relative complex boundary layer events such as transition, turbulence, flow separation, dynamic stall which is still the object of many researches. One challenge is the flow prediction based on RANS codes together with experimental developments in such complex unsteady flows. Srinivasan et al. [2] and Barakos [3] showed the accuracy of RANS codes for the prediction of hydrodynamic loading of foils in case of low angles of incidence; they also highlighted the influence of turbulence model when flow separation is strong at high angles of incidence. The influence of pitching velocities can be also of primary importance on loading prediction for flows at low Reynolds numbers. Hamdani and Sun [4] showed in a numerical study that inertial effects increased when pitching velocities increased at low Reynolds numbers. Lee and Gerontakos [5] developed an experimental study for an oscillating airfoil at various reduced frequencies $\kappa = \dot{\alpha}c/2U_\infty$ (with $\dot{\alpha}$ the pitching velocity) at $Re = 1.35 \times 10^5$. The reduced

* Corresponding author. Tel.: +33 2 98 23 38 57.
E-mail address: antoine.ducoin@ecole-navale.fr (A. Ducoin).

0997-7546/$ – see front matter © 2009 Elsevier Masson SAS. All rights reserved.
doi:10.1016/j.euromechflu.2009.06.001

Nomenclature

b	hydrofoil span
c	hydrofoil chord
C	convective term
D	diffusive term
h	tunnel test section height
k	low frequency cut-off
Re	Reynolds number ($=U_\infty c/\nu$)
$Re_{\theta t}$	transition Reynolds number
$S_{t\theta}$	Strouhal number of LSB ($=f(\theta)_{sep}/(v_e)_{sep}$)
p	local fluid pressure
P_0	reference pressure
u_τ	friction velocity
U_∞	free stream velocity
v	local fluid velocity
$\mathbf{v}$	fluid velocity vector
$\mathbf{v}^*$	grid velocity vector
$(v_e)_{sep}$	external velocity, laminar separation
y^+	dimensionless wall distance ($=yu_\tau/\nu$)

Greek letters

α	angle of incidence
$\dot{\alpha}$	pitching velocity
$\dot{\alpha}^*$	dimensionless pitching velocity
β	relaxation factor
φ	unknown fluid scalar
γ	intermittency
Γ	boundary of a control volume
κ	reduced frequency
Λ_ϕ	diffusion term
μ	dynamic viscosity
ν	fluid kinematic viscosity ($=\mu/\rho$)
$(\theta)_{sep}$	momentum thickness, laminar separation
ρ	fluid density
Σ_ϕ	source term
Ω	control volume

frequency is a reliable parameter to characterize unsteady pitching velocity effect. For small reduced frequencies, boundary layer events produce variations in lift, drag and moment coefficients. For instance, boundary layer transition caused by laminar separation is delayed and promoted when reduced frequencies increases. The lift coefficient and lift-curve slope exhibit modifications but it was shown that the laminar separation bubble length was independent on the reduced frequency.

The case of laminar separation induced transition has been studied extensively in many works concerning aerodynamic applications. For hydrofoils at moderate Reynolds number, it appears near the trailing edge for moderate angle of incidence and suddenly moves toward the leading edge as the angle of incidence increases to form a laminar separation bubble that induces flow transition. Tani [6] showed that the bubble length is reduced when the adverse pressure gradient increases. Many works have been therefore considered on laminar separation bubble (LSB) from the pioneer experimental works of Gaster [7] to recent DNS simulations like Alam and Sandham [8] and Alving and Fernholz [9]. The latter show that complex and multi scaled structures can occur in the LSB wake. Pauley et al. [10] studied an unsteady laminar separation bubble induced by an adverse pressure gradient on a leading-edge geometry. It has been found that the frequency of the vortex shedding from the bubble can be non-dimensionalized using a Strouhal number $S_{t\theta}$ based on momentum thickness $(\theta)_{sep}$ and external velocity $(v_e)_{sep}$ at laminar separation which appears in many recent works [11,12]. Moreover, some recent DNS studies have shown that those vortex sheddings resulting into a flapping motion of the bubble generate characteristic velocity and pressure fluctuations downstream the bubble, as highlighted by Rist and Maucher [13] in the case of a flat plate and Jones et al. [14] in the case of an airfoil.

Recent works focus on the impact of laminar-to-turbulent transition modeling in RANS codes for unsteady flows. Smith et al. [15] show that fully turbulent computations over predict lift and drag. Shelton et al. [16] included a transition model and showed its impact on hydrodynamic coefficients which is closer from experiments compared to fully turbulent computations; transition models can also be important for stall prediction. As shown, there is a real challenge to introduce complex flow features in RANS code and to develop experimental methods to a better understanding of unsteady flows.

The present paper focuses on the a flow over an hydrofoil undergoing a transient pitching motion at a moderate Reynolds number $Re = 0.75 \times 10^6$. Both experimental and numerical approaches were developed. The experiment consist in measuring the wall pressure using pressure transducers at several points located along the chord on the suction side of the hydrofoil. Computations are led with the CFD RANS based code *CFX*© in the same conditions as in the experiment. One aim of the study is a better understanding of boundary layer events like transition and laminar separation induced transition on an hydrofoil suction side undergoing a forced transient motion at various pitching velocity. An other point is to check the accuracy and the limitations of a RANS simulation in the flow prediction. The flow is studied in the case of a low pitching velocity corresponding to a quasi-static motion. Measured and computed wall pressures near the leading edge and the trailing edge help to characterize separation and transition location on the hydrofoil. Then the influence of the pitching velocity on the boundary layer events is investigated. Finally the effects of the pitching velocity on the hydrodynamic loading are highlighted on the basis of the numerical study.

2. Experimental set up

Measurements are carried out in the cavitation tunnel at IRENav. The test section is 1 m long and has an square section of $h = 0.192$ m. The velocity can range between 0 and 15 m/s and the pressure from 30 mbar to 3 bars. The hydrofoil is a NACA66 witch presents a camber type NACA $a = 0.8$, a camber ratio of 2% and a relative thickness of 12% [17]. It is mounted horizontally in the tunnel test section (Fig. 1). The chord is $c = 0.150$ m and the span is $b = 0.191$ m. It corresponds to a low aspect ratio $b/c = 1.3$ and a confinement parameter $h/c = 1.28$ that can imply relatively complex 3D effects and blocking effects that are difficult to quantify. Moreover it could implicate flow separation on the horizontal wall tunnel for large angles of incidence. However no indication of such phenomena was observed in the present study. Particularly no specific cavitation patterns that could reveal boundary layer separation on the wall was observed. On the other hand the vertical walls induce the development of boundary layers interacting with the foil surface in the vicinity of the tip and the root of the hydrofoil. It was observed that the wall boundary

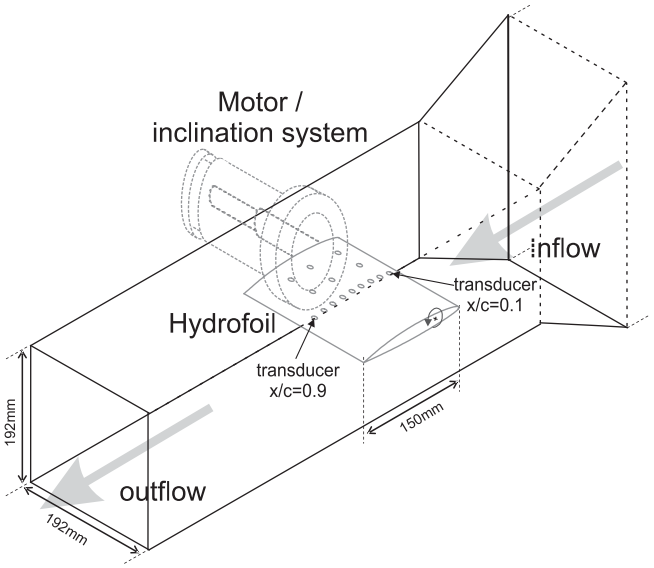

Fig. 1. Hydrofoil instrumentation and tunnel test section.

layer thickness were of about 0.009 m for a free stream velocity of 5 m/s corresponding to about 10% of the span. Moreover, flow visualizations based on the cavitation inception on the suction side show that about 80–90% of the foil surface can be considered as a 2D flow [18], depending on the angle of incidence.

Pressure measurements are carried out using seventeen piezo-resistive transducers (Keller AG 2 MI PAA100-075-010) of 10 bars maximum pressure. The pressure transducers are mounted into small cavities with a 0.5 mm diameter pinhole at the hydrofoil surface. The wall-pressure spectrum measured by the transducer is attenuated from the theoretical cut-off frequency $f_c = 9152$ Hz. Experiments are led with a sample frequency of $f = 20$ kHz.

The transducer locations are given in Fig. 1. As shown, one set of ten transducers is aligned along the chord on the suction side at mid-span, starting from the leading edge at reduced coordinate $x/c = 0.1$ up to the trailing edge at coordinate $x/c = 0.90$ with a step of 0.10c. Two sets of three transducers are arranged parallel to this line in order to analyze three-dimensional effects (which is however beyond the scope of this paper).

The paper presents some measurements in which a roughness patch has been added near the leading edge. This allows the suppression of the transition to turbulence zone and laminar separation bubble. The patch has 16 μm grain and is 250 μm thick.

The nominal free stream velocity U_∞ is 5 m/s, corresponding to a Reynolds number based on the foil chord length of $Re = 0.75 \times 10^6$. The uncertainty for the free stream velocity is $\Delta U_\infty = \pm 0.02$ m/s. The pressure in the tunnel test section was set to $P_0 = 1.4$ bars with an uncertainty of $\Delta P_0 = \pm 0.003$ bar. This pressure condition allows to avoid cavitation which is therefore not considered in the study. The hydrofoil pitches about an axis located at 25% from the leading edge. The angle of incidence varies from 0° to 15° and then comes back to 0°, with at least two periods of acceleration and 2 periods of deceleration. The major uncertainty comes from the zero angle of incidence which is adjusted by aligning the foil chord to the horizontal top wall of the test section; it is about $\Delta\alpha = \pm 0.15°$. As shown in Fig. 2, four pitching velocities are defined, from a considered low pitching velocity to a high pitching velocity.

The average rotation velocity is $\dot{\alpha} = 2\alpha_{\max}/t_f$, where t_f is the total time of transient motion. A similarity parameter based on the chord length c and the upstream velocity U_∞ is introduced to characterize the pitching velocity: $\dot{\alpha}^* = \dot{\alpha} \times c/U_\infty$.

In some cases, the pressure signal is decomposed using the "Empirical Mode Decomposition "(EMD) [19], which has been the object of several hydrodynamic studies [20,21]. This method consists on the decomposition of an unsteady signal $x(t)$ into intrinsic oscillatory components called "Intrinsic Mode Functions"(IMFs) by means of an algorithm called sifting process. The basic principle is the extraction of intrinsic time scale components of the signal starting from finer temporal scales (high frequency modes) to coarser ones (low frequency modes). The total sum of the extracted IMFs matches the signal and therefore ensures signal complete reconstruction. Huang et al. [19] have introduced the EMD method for analyzing data from unsteady and non-linear processes. In the present paper, the method is used first for the reconstruction of a low frequency signal $\overline{x}(t)$ in order to obtain a trend signal. On one hand, it permits a more pertinent comparison with computations which are resolved with RANS equations. On the other hand, the medium and high frequency components are used to reconstruct a signal $\tilde{x}(t)$ in order to analyze the pressure fluctuations with spectrograms. Then the reconstructed signal can be written as [22]:

$$\overline{x}(t) = \sum_{j=k}^{n} \mathrm{IMF}_j(t) + r_n(t) \tag{1}$$

$$\tilde{x}(t) = \sum_{j=1}^{k-1} \mathrm{IMF}_j(t) \tag{2}$$

where n is the number of modes, $r_n(t)$ is the residue, and k is the low frequency cut-off [19].

An example is shown in Fig. 3 where the reconstructed pressure signal $\overline{C_P}(t)$ corresponds to low frequency modes whereas the reconstructed pressure signal $\widetilde{C}_P(t)$ corresponds to medium and high frequency modes for $k = 10$.

Experimental frequencies resulting from wall-pressure fluctuations relied to LSB are then non-dimensionalized using the dimensionless shedding frequency of Pauley et al. [10]. It is based on boundary layer momentum thickness $(\theta)_{sep}$ and local free stream velocity $(v_e)_{sep}$ at the laminar separation point, those quantity being determined experimentally, and it can be written as $S_{t\theta} = f(\theta)_{sep}/(v_e)_{sep}$. In this paper the Strouhal number is computed by numerical values of $(\theta)_{sep}$ and $(v_e)_{sep}$ and experimental value of the frequency. It is then compared with the Strouhal number $S_{t\theta} = 0.00686$ [10].

3. Flow modeling and numerical resolution

The fluid problem is solved with the finite volume technique using the CFD code *CFX*©. The fluid flow is described by the mass and momentum conservation equations which read for an incompressible and viscous fluid:

$$\frac{\partial v_j}{\partial x_j} = 0 \tag{3}$$

$$\frac{\partial(\rho v_i)}{\partial t} + \frac{\partial(\rho v_i v_j)}{\partial x_j} = -\frac{\partial p}{\partial x_i} + \mu \frac{\partial^2 v_i}{\partial x_j \partial x_j} \tag{4}$$

where v is the fluid velocity, ρ is the fluid density, p is the pressure and μ is the dynamic viscosity.

Equations of mass and momentum are integrated over a control volume Ω of boundary Γ, using the Leibnitz rule and the Gauss

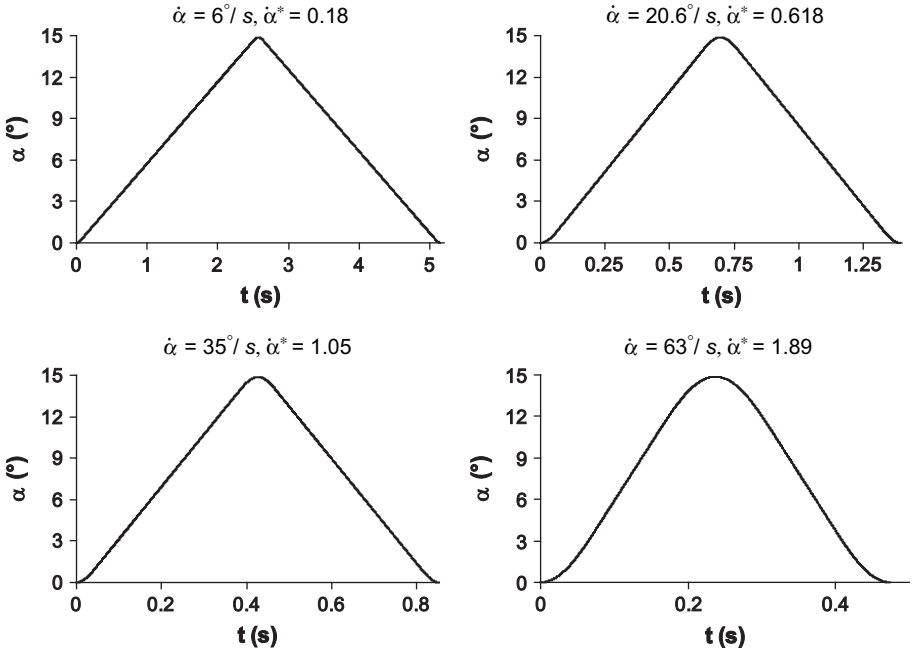

Fig. 2. Measurements and computations, angle of incidence versus time for 4 pitching velocities.

theorem. The general form of an integrated conservation equation for a scalar fluid unknown φ is the following one:

$$\frac{\mathrm{d}}{\mathrm{d}t}\left(\int_{\Omega}\rho\phi\mathrm{d}\Omega\right)+\int_{\Gamma}\rho\phi\mathbf{v}\cdot\mathbf{n}\mathrm{d}\Gamma=\int_{\Omega}\Sigma_{\phi}\mathrm{d}\Omega+\int_{\Gamma}\Lambda_{\phi}\nabla\phi\cdot\mathbf{n}\mathrm{d}\Gamma \quad (5)$$

where Σ_ϕ denotes a source term for quantity ϕ and Λ_ϕ stands for the diffusion of quantity ϕ. The time dependent terms are approximated by a second order backward Euler scheme:

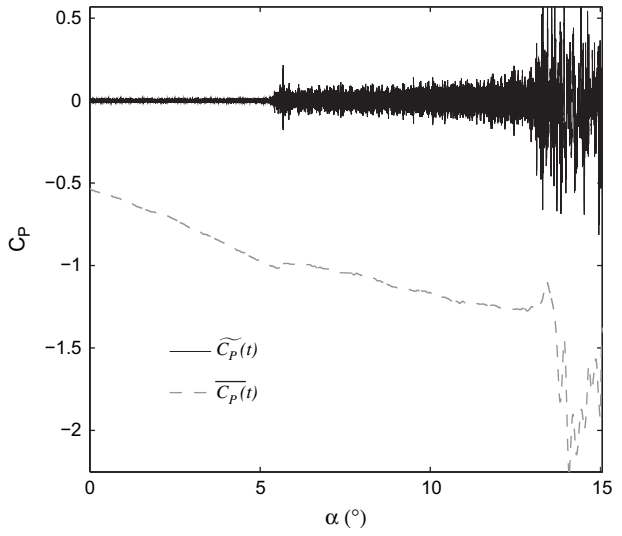

Fig. 3. Measurement, reconstructed pressure signal by EMD method, $\overline{C_P}(t)$ (Eq. (1)) and $\widetilde{C_P}(t)$ (Eq. (2)), $\dot{\alpha}^* = 0.18$.

$$\frac{\mathrm{d}}{\mathrm{d}t}\left(\int_{\Omega}\rho\phi\mathrm{d}\Omega\right)\approx\frac{\rho|\Omega|}{\delta t}\left(3/2\phi_P^{n+1}-2\phi_P^{n}+1/2\phi_P^{n-1}\right) \quad (6)$$

where n, $n-1$ and $n+1$ are the time steps.

The convective and diffusive terms respectively denoted as C and D are calculated using finite difference approximations, leading to the global expression:

$$\int_{\partial\Omega}\rho v_j\phi-\Lambda_{\phi}\frac{\partial\phi}{\partial x_j}\mathrm{d}n_j\approx\sum_{M}C_M^{n+1}\phi_M^{n+1}-D_M^{n+1}\phi_M^{n+1} \quad (7)$$

where M stands for the neighboring points of cell Ω_P. Nodal values are computed with a high resolution upwind scheme. This advection scheme is implemented into the CFD code and can be cast in the form:

$$\phi_p=\phi_{up}+\beta\nabla\phi\Delta\overrightarrow{r} \quad (8)$$

where ϕ_p and ϕ_{up} are respectively the values of ϕ at the integration point P and at the upwind node (depending on the flow direction). β is a relaxation coefficient ranging between 0 and 1. The high resolution scheme computes β locally in order to be as close to 1 as possible without violating boundedness principles, see Barth and Jesperson [23]. $\overrightarrow{r}$ is the vector from the upwind node to the integration point P. A value of $\beta=1$ leads to a second order upwind difference scheme whereas a value of $\beta=0$ leads to a first order upwind difference scheme. Taking into account Eqs. (7) and (8) leads to the following algebraic non-linear system:

$$A_P\phi_P^{n+1}+\sum_{N}A_N\phi_N^{n+1}=b_P^n \quad (9)$$

where P stands for any cell node and N for all neighboring nodes. The latter equation can be formulated as $\mathbf{A}(\phi)\boldsymbol{\phi}=\mathbf{b}$; the non-linear system can be solved with iterative methods and yields the value of quantity φ at each node of the fluid mesh. In the present study, the

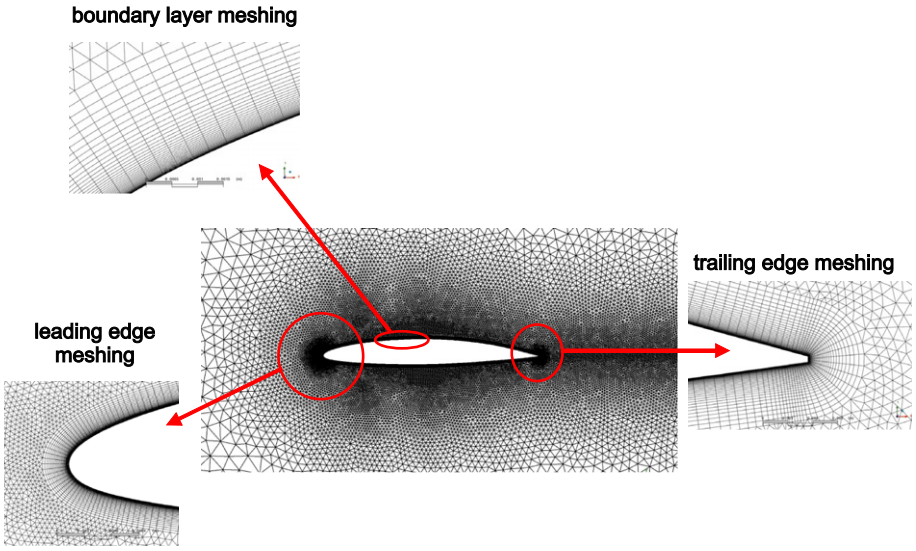

Fig. 4. Mesh of the fluid computational domain.

numerical calculation of the fluid flow has to take into account modification of the computational domain, which results from the forced pitching motion of the hydrofoil. The simulation is therefore based on the ALE formulation of the conservation equations, which reads:

$$\frac{\mathrm{d}}{\mathrm{d}t}\left(\int_{\Omega}\rho\phi\,\mathrm{d}\Omega\right)+\int_{\Gamma}\rho\phi\left(\mathbf{v}-\mathbf{v}^{*}\right)\cdot\mathbf{n}\,\mathrm{d}\Gamma = \int_{\Omega}\Sigma_{\phi}\,\mathrm{d}\Omega+\int_{\Gamma}\Lambda_{\phi}\nabla\phi\cdot\mathbf{n}\,\mathrm{d}\Gamma \tag{10}$$

for unknown ϕ. $\mathbf{v}^{*}$ is the so-called "grid velocity" which accounts for the displacement of the nodes in the fluid mesh. As this new unknown in the fluid problem is introduced, an additional conservation equation has to be solved, namely The Space Conservation Law (SCL), which ensures that no artificial fluid flow is generated by the mesh motion [24]. The SCL reads:

$$\frac{\mathrm{d}}{\mathrm{d}t}\left(\int_{\Omega}\mathrm{d}\Omega\right)=\int_{\Gamma}\mathbf{v}^{*}\cdot\mathbf{n}\,\mathrm{d}\Gamma \tag{11}$$

It is solved once the displacement of the node in the fluid mesh is imposed and it yields the grid velocity. Displacement of the node is the fluid mesh allows taking moving boundaries into account; many remeshing techniques are available, among which the shear slip mesh update method [25,26] and the ortho-semi torsional method [27]. In the *CFX*© code, the latter method is employed to perform the moving mesh simulation.

3.1. Turbulence and transition modeling

The calculations are performed with the CFD RANS based code *CFX*©. The $k-\omega$ *SST* (Shear Stress Transport) model appears to be an accurate turbulence model for boundary layer detachment prediction [28–30].

The $k-\omega$ *SST* turbulence model is coupled with a transition model $\gamma - Re_{\theta}$ which uses experimental correlations based on local variables [31–33]. The model is based on two transport equations. The first one is for intermittency γ which triggers the transition process:

$$\frac{\partial(\rho\gamma)}{\partial t}+\frac{\partial(\rho v_j\gamma)}{\partial x_j}=P_{\gamma}+E_{\gamma}+\frac{\partial}{\partial x_j}\left[\left(\mu+\frac{u_{\tau}}{\sigma_f}\right)\frac{\partial\gamma}{\partial x_j}\right] \tag{12}$$

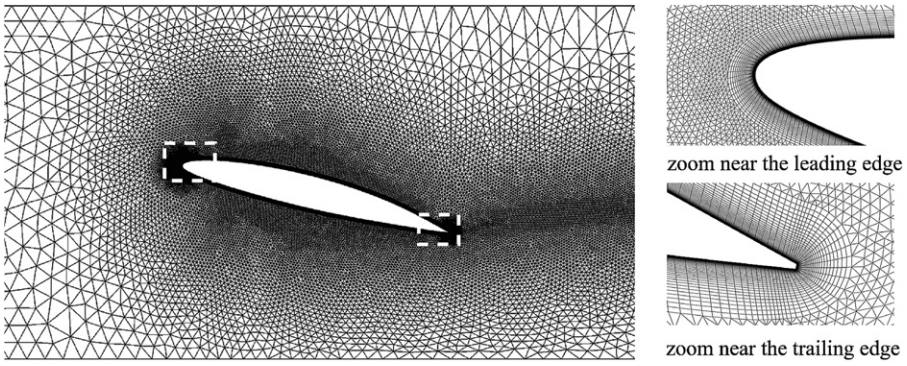

Fig. 5. Mesh of the fluid computational domain after deformation, $\alpha = 15°$.

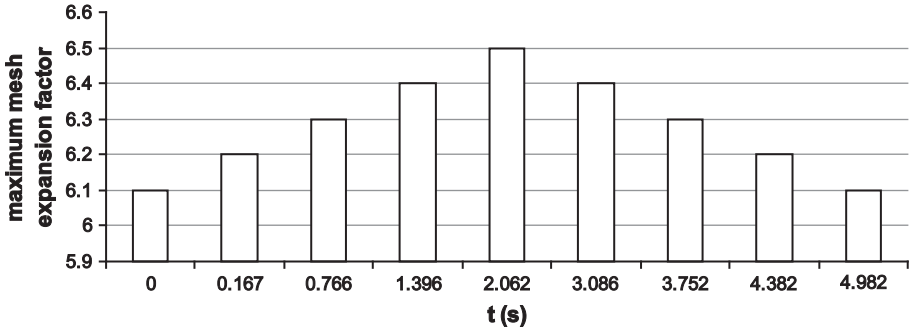

Fig. 6. Mesh expansion factor versus time.

where P_γ and E_γ are the transition sources based on empirical correlations [31]. u_τ is the friction velocity and σ_f is a constant.

The second one is a transport equation for the transition momentum thickness Reynolds number $\overline{Re_{\theta t}}$ is given by:

$$\frac{\partial(\rho\overline{Re_{\theta t}})}{\partial t}+\frac{\partial(\rho v_j\overline{Re_{\theta t}})}{\partial x_j}=P_{\theta t}+\frac{\partial}{\partial x_j}\left[\sigma_{\theta t}(\mu+u_\tau)\frac{\partial\overline{Re_{\theta t}}}{\partial x_j}\right] \tag{13}$$

with $P_{\theta t}$ a source term which forces $\overline{Re_{\theta t}}$ to match the local value of $Re_{\theta t}$ based empirical correlation and $\sigma_{\theta t}$ is a source term of diffusion control.

In this formulation, only local information is used to activate the production term in the intermittency equation. This model allows to capture major transition effects and is accurate in the case of separation induced transition. The intermittency is modified to accept values larger than one at separation in order to have a correct prediction of transition length. Complete transition model formulation is given in Ref. [33].

3.2. Boundary conditions and discretization

The 2D domain corresponds to the tunnel test section at IRENav. The inlet velocity is set to $U_\infty = 5$ m/s and the taken outlet reference pressure is set to zero. A no slip condition is imposed on the hydrofoil surface and the symmetry conditions on the top and bottom walls of the tunnel are chosen for simplification, in order to have a coarse mesh in this zone to allow large deformations. This can have some influence on the prediction of simulation as shown recently by Dular et al. [34] due to non uniformity of the upstream flow in the real situation. However numerical computations were performed taken into account of the side wall boundary layers in static cases and have shown a weak influence. For an angle of incidence of 10° the difference of the pressure coefficient on the hydrofoil suction side was lower than 1% when tunnel wall boundary layers were considered. Moreover from an experimental point of view, the boundary layer thickness on the tunnel walls are found to be of about 8–9 mm for a free stream velocity of about 5 m/s. This indicates that the real upstream velocity profile is uniform in the large part of the test section. Transient computations are initialized with a stationary converged computation. As shown in Fig. 4, the mesh is composed of 66 000 elements and 50 layers are used in the structured near wall zone. The other part of the domain is discretized with unstructured triangle elements. The boundary layer is discretized in order to satisfy $y^+ = 1$, which ensures a low Reynolds resolution. Mesh refinements are performed at the leading edge, at the trailing edge and in the wake. The hydrofoil motion is taken into account using a changing boundary condition at the wall: foil mesh coordinates are calculated at each time step and the whole domain is then meshed again by moving each node. This technique uses a diffusivity parameter applied in the mesh displacement equation which induces a mesh stiffness [35–37]. This one is set to be inversely proportional to the wall distance in order to limit mesh distortion in the wall region. A view of the deformed mesh is shown in Fig. 5 for the maximum angle of incidence $\alpha = 15°$. As shown, mesh distortion is small in the near wall region and cells have the same areas as the initial mesh, unless the normal to the wall has moved of about few degrees, see the difference between Figs. 4 and 5. Far away from the hydrofoil, cells are highly extended near the top wall and highly compressed near the bottom wall. Moreover, the quality of the deformed mesh stays very close to the quality of the initial mesh as shown by the evolution of the maximum expansion factor in Fig. 6. The RANS equations are solved in an arbitrary referential with the Arbitrary Lagrangian Euler (ALE) formulation [36].

Mesh convergence is carried out on hydrodynamic coefficients for an angle of attack of 6° and a steady flow. Table 1 summarizes the lift and drag coefficients for each tested mesh case. The thickness of the structured mesh near the wall and the aspect ratio between structured and unstructured meshes have been kept. On one hand, it appears that wall function predicts the lift coefficient quite well as compared to the low Reynolds resolution $y^+ = 0.3$ taken as a reference. On the other hand, the wall functions under predict the drag coefficient of about 15%. This is due to the contribution of wall shear to the drag coefficient. The influence of the number of elements has been investigated in Table 2. N_{foil} is the number of nodes on the hydrofoil surface and N_{total} is the total number of elements. The lift coefficient converges very fast, from $N_{foil} = 100$, while the drag coefficient converges from $N_{foil} = 200$.

Table 1
Computations, lift and drag coefficients convergence according to boundary layer resolution, $\alpha = 6°$, $Re = 750\,000$.

Boundary layer resolution	y^+	C_l	(%)	C_d	(%)
Wall function	50	0.9661	3.3	0.0144	14.6
Low Reynolds	2	0.9529	1.9	0.0163	3.2
Low Reynolds	1	0.9503	1.6	0.0164	2.7
Low Reynolds	0.5	0.9362	0.1	0.01676	0.5
Low Reynolds	0.3	0.9353	–	0.01686	–

Table 2
Computations, lift and drag coefficients as functions of number of elements $\alpha = 6°$, $Re = 750\,000$.

N_{foil}	N_{total}	C_l	(%)	C_d	(%)
50	18 000	0.9915	4.3	0.02198	34.2
100	23 000	0.9545	0.4	0.01987	21.3
200	40 000	0.9477	0.3	0.01719	4.9
400	66 000	0.95026	0.1	0.0164	0.1
$N_{max} = 800$	100 000	0.95082	–	0.01638	–

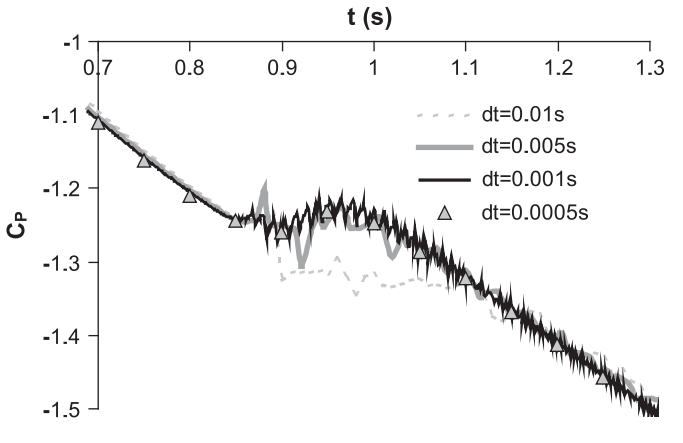

Fig. 7. Computations, pressure coefficient versus time for various time steps during transition, $\dot{\alpha}^* = 0.18$, $Re = 750\,000$.

Temporal discretization has been set according to CFL number with fixed spatial mesh. Fig. 7 shows pressure coefficients located at $x/c = 0.1$ versus time for pitching motion from 0° to 15° and $\dot{\alpha}^* = 0.18$. The study focuses on the non-linear behavior which appears from $t = 0.9$ s to $t = 1$ s: it is associated to laminar to turbulent transition. It needs a high temporal discretization level: convergence is indeed obtained for values lower than $\Delta t = 0.001$ s. In the same way, Fig. 8 shows the pressure coefficient when leading-edge separation occurs. It is found to be very sensitive to Δt. For the highest Δt, there is an advance of separation whereas $\Delta t = 0.001$ s and $\Delta t = 0.0005$ s give same results: $\Delta t = 0.001$ s has therefore been chosen for the pitching velocity of $\dot{\alpha}^* = 0.18$. A minimum number of time steps is set to correctly take into account the dynamic in computation. The time step Δt satisfies the condition $\Delta t/t_f < 5 \times 10^{-4}$, where t_f is the total simulation time which depend of pitching velocity.

4. Results and discussion

Fig. 9a shows the measured pressure coefficient at $x/c = 0.3$ during the transient motion from 0° to 15° for $\dot{\alpha}^* = 0.18$ compared to the computed value. There is a good agreement between the experimental and the numerical results except for high frequency fluctuations which are not captured by the simulation.

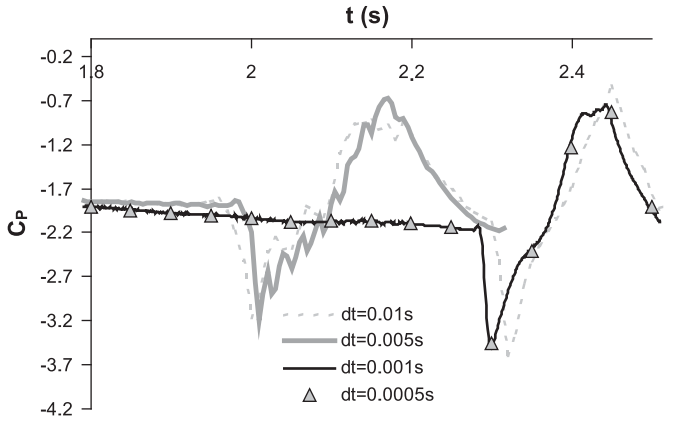

Fig. 8. Computations, pressure coefficient versus time for various time steps in leading-edge separation zone, $\dot{\alpha}^* = 0.18$, $Re = 750\,000$.

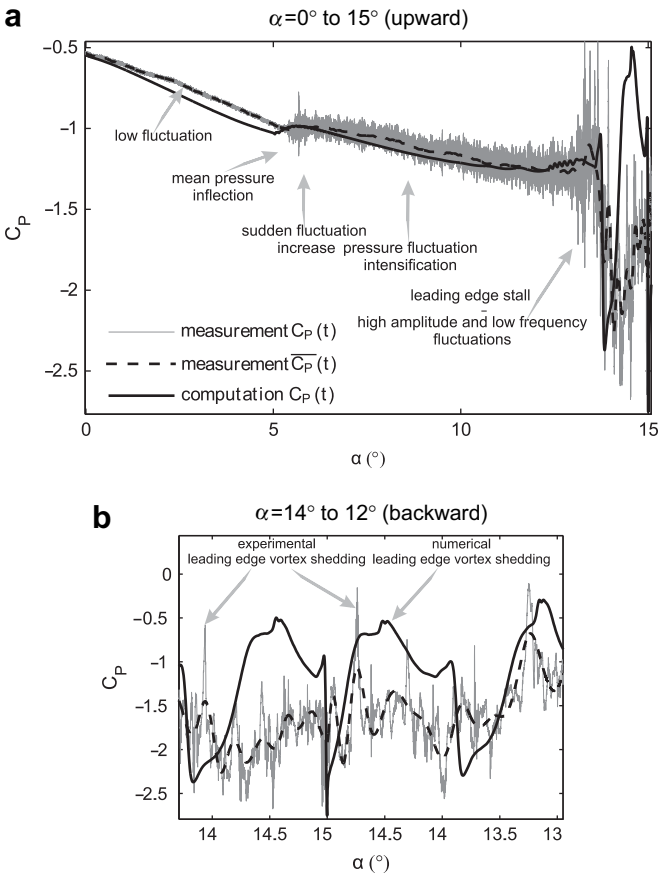

Fig. 9. Experimental and numerical pressure coefficient as function of the angle of incidence at $x/c = 0.3$ during the transient motion, $\dot{\alpha}^* = 0.18$, $Re = 750\,000$.

From 0° to 5°, the pressure decreases with low fluctuations. At 5°, the pressure stops to decrease and shows an inflection with a high level of fluctuations. Then the pressure continues to decrease with significant fluctuations, increasing from 6° to 13°. A more accurate analysis showed that the fluctuations are quasi-periodic and can be related to vortex shedding downstream a laminar separation bubble. From 13° a strong pressure overshoot followed by low frequency fluctuations ($f \approx 6$ Hz) with large amplitude are observed resulting of stall, as shown in Fig. 9b. Again, the higher frequency fluctuations are not captured by computations whereas the periodic peaks resulting from the leading-edge vortex shedding are well reproduced. The relatively complex characteristic of the wall-pressure evolutions comes from the various features of the boundary layer flow during foil rotation.

4.1. Flow analysis

The flow is first analyzed for the lowest pitching velocity $\dot{\alpha}^* = 0.18$ considered as a quasi-static case. Fig. 10 shows the experimental and computed wall-pressure coefficients evolutions for transducers located from $x/c = 0.2$ to $x/c = 0.9$. As shown, there is a good agreement between computations and measurements on wall pressures. A maximum difference of about $\Delta C_P = 0.1$ is found at $x/c = 0.9$, $x/c = 0.7$ and $x/c = 0.2$. Measured wall-pressure coefficient at $x/c = 0.9$ shows high level fluctuations which move and increase to $x/c = 0.8$ at $\alpha \approx 2°$ and then to $x/c = 0.7$ at $\alpha \approx 4°$ as shown in Fig. 10b, c. Computations show a global increase of pressure coefficient without any fluctuation due to a laminar separation bubble which moves from the trailing edge to the leading edge.

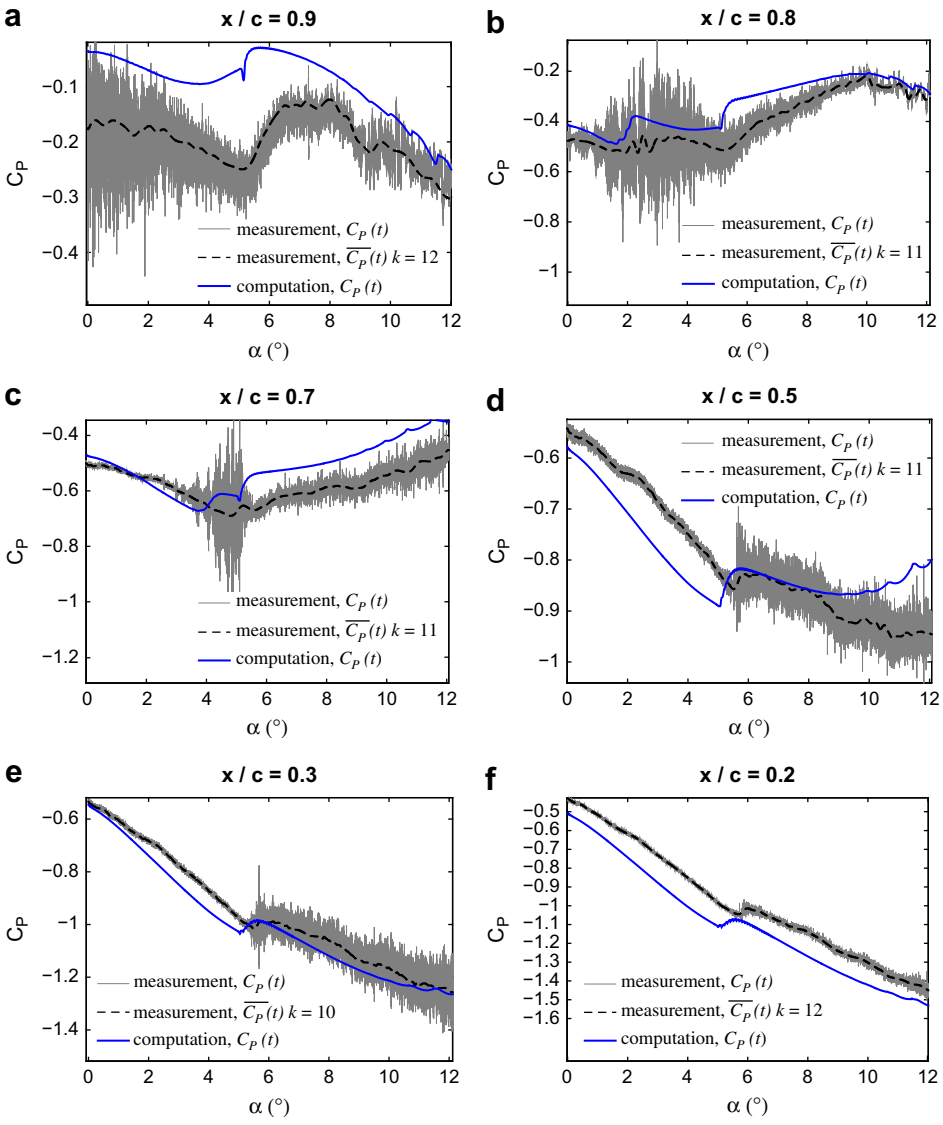

Fig. 10. Experimental and numerical pressure coefficient versus angle of incidence during the hydrofoil rotation at $\dot{\alpha}^* = 0.18$ for various transducers along the suction side, $\alpha = 0$–12° before stall. The dotted lines are the low frequency EMD pressure signals $\overline{C_P}(t)$ (Eq. (1)), $Re = 750\,000$.

This induces a strong temporal variation of pressure due to the constant pressure zone in the LSB region. For both computation and measurement, there is a net pressure inflection for $\alpha = 5.7^\circ$ as transition is moving toward the leading edge. Fig. 10d–f shows that the measured pressure fluctuations highly increase up to a burst and continue to increase progressively to $\alpha = 12^\circ$. Spatially, the level of fluctuations increases from $x/c = 0.2$ to $x/c = 0.5$. At the same time, wall-pressure coefficient at $x/c = 0.9$ and $x/c = 0.8$ reaches a maximum value at respectively $\alpha = 7^\circ$ and $\alpha = 10^\circ$ compared to $\alpha = 5.5^\circ$ and $\alpha = 10^\circ$ according to computations. It corresponds to the trailing-edge separation passing on the pressure transducers (Fig. 12) for which the flow is decelerated and then accelerated by the reverse flow.

This experimental versus computation wall-pressure analysis enables a validation of the simulation on local phenomena which event in the boundary layer (such as transition by laminar separation bubble and leading-edge vortex shedding). From now on, the analysis will therefore be based on numerical simulations which are assumed to correctly reproduce the experimental flow.

Fig. 11 shows the velocity streamlines determined from computations. As shown at 0°, a reversed flow is located at $x/c = 0.8$ resulting from a laminar separation bubble (LSB) inducing a transition to turbulent flow at reattachment. The displacement of LSB toward the leading-edge zone is observed up to 5°. At 5° the LSB at trailing edge is replaced by a LSB at leading edge and stays close to this location when the angle of attack increases, as shown in Fig. 11 for $\alpha = 11^\circ$. Then, stall is observed for 13.6° together with leading-edge vortex shedding. At $\alpha = 13.9^\circ$, a vortex extends along the suction side corresponding to the strong global pressure overshoot, as shown on Fig. 9. Then two contra-rotative vortices are shed from the trailing edge ($\alpha = 14.2^\circ$). This scenario is repeated 3 times periodically in the case of the lowest pitching velocity. A reverse scenario is observed during downward rotation.

Separation and transition points have been located using the "wall shear stress equal to 0 criteria". The transition point is defined as the turbulent reattachment point [33]. Fig. 12 summarizes the locations of the separations, reattachment and transition points from $\alpha = 0^\circ$ to 13° before stall. The vertical axis is the x/c location

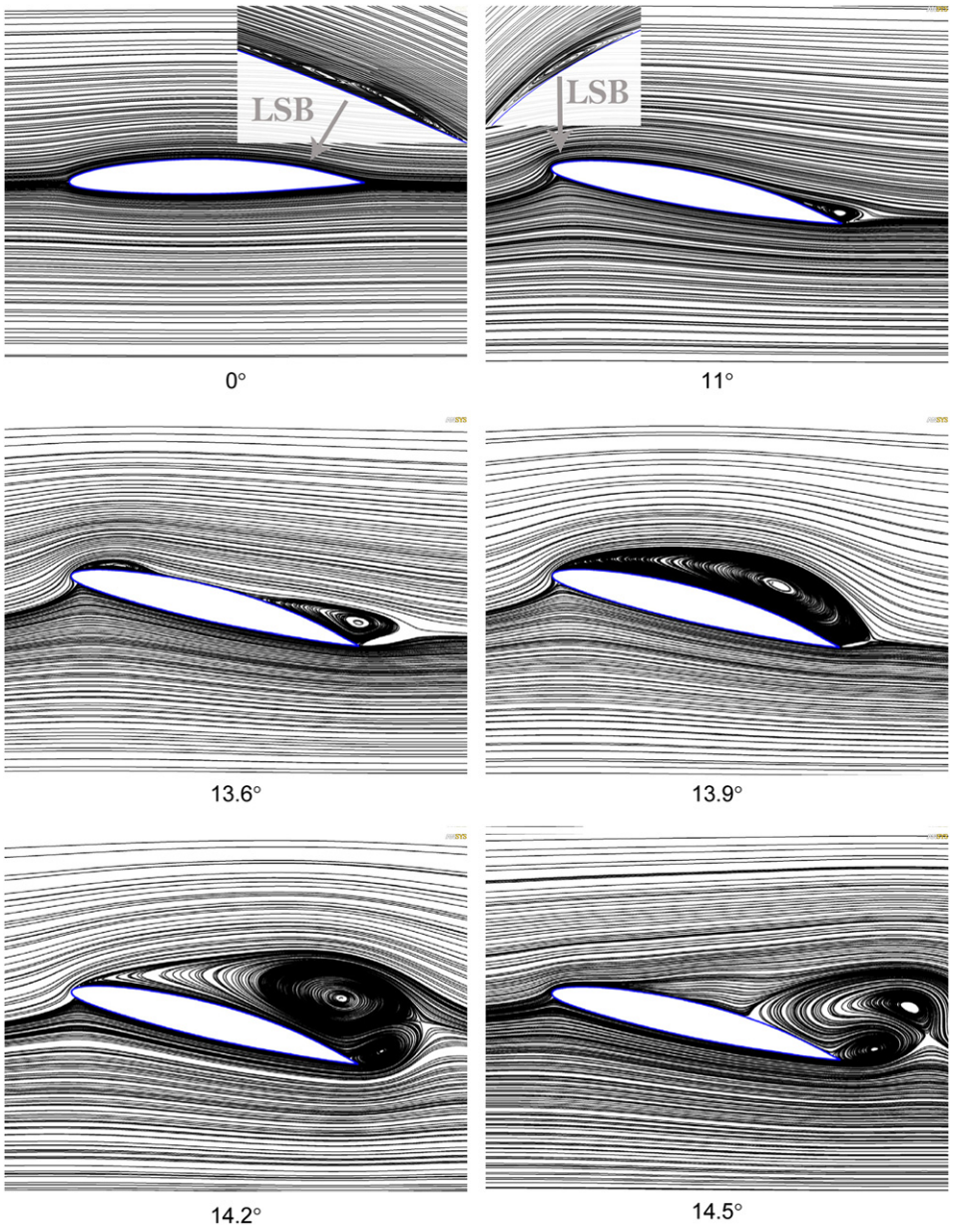

Fig. 11. Computation, flow visualizations, $\dot{\alpha}^* = 0.18$, including laminar separation bubble (LSB), $Re = 750\,000$.

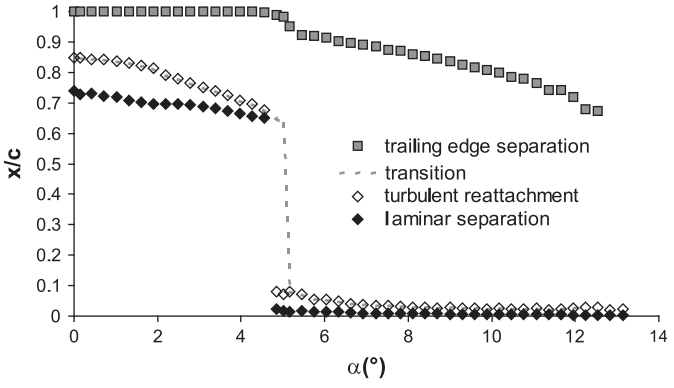

Fig. 12. Computation, location of separations, reattachment and transition points on the suction side as functions of the angle of incidence during the hydrofoil rotation, $\alpha = 0$–$13.4°$, $Re = 750\,000$, $\dot{\alpha}^* = 0.18$.

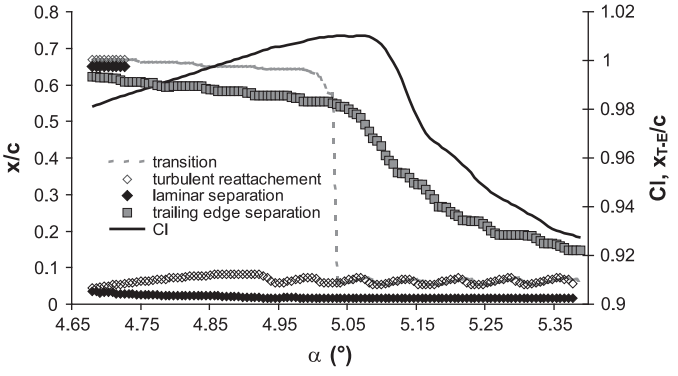

Fig. 13. Computation, location of separations, reattachment and transition points on the suction side as functions of the angle of incidence during the hydrofoil rotation, $\alpha = 4.65$–$5.4°$, $Re = 750\,000$, $\dot{\alpha}^* = 0.18$.

along the chord from leading edge ($x/c=0$) to trailing edge ($x/c=1$). The trailing-edge separation point is located very close to the trailing edge for 0°, and moves slowly toward the leading edge when the angle of incidence increases. For $\alpha=0°$ to 5° the two characteristic points (laminar separation and turbulent reattachment) are respectively located between $(x/c)_{sep}=0.74$–0.66 and $(x/c)_{reattach}=0.85$–0.69. As a matter of fact, the global length of LSB tends to decrease as α increases. At these angles of incidence, the boundary layer around the hydrofoil is laminar. As shown in Fig. 13, at $\alpha=4.7°$, the trailing-edge LSB disappears and a shorter LSB induced by higher pressure gradient appears at the leading edge which induces a shift of the transition location from $x/c=0.66$ to $x/c=0.08$ at $\alpha=5°$. Then the boundary layer around the hydrofoil is fully turbulent. As well, the trailing-edge separation x_{T-E} shift from $x/c=0.99$ to $x/c=0.92$ and leads to a lift coefficient decrease from $C_L=1.01$ to $C_L=0.93$.

Experimental high level of fluctuations related in Fig. 10 have a periodic behavior. Fig. 14a–c shows a frequency $f_{11}=550$ Hz that disappears at $t=0.92$ s corresponding to $\alpha=5.5°$. The frequency results from a global instability in the reattachment region [38]. This leads to a flapping motion of the separated shear layer where vortex shedding occurs in the LSB wake. It moves from transducers $x/c=0.9$ to $x/c=0.7$ because the LSB is moving progressively to the leading edge as the angle of incidence increases. Higher frequencies visible in Fig. 14a and mostly Fig. 14b are harmonics of $f_{11}=550$ Hz. A peak is visible after $t=0$ s at $f_{12}\approx 1100$ Hz for $x/c=0.9$ and moves up to $x/c=0.8$ at $t=0.35$ s. Other harmonics are clearly visible at $t=0.45$ s for $x/c=0.8$, values are $f_{12}\approx 1100$ Hz, $f_{13}\approx 1650$ Hz and $f_{14}\approx 2100$ Hz. Those frequencies result from a turbulence development induced by global instability at $f_{11}=550$ Hz. Haggmark et al. [38] found that disturbance over LSB can induce low and high frequency fluctuations.

Fig. 14e shows a frequency of $f_2=1700$ Hz which is clearly identified as a transition shift at the leading edge. This frequency is also interpreted as a vortex shedding frequency induced by LSB at leading edge. The transducer located upstream at $x/c=0.2$ shows

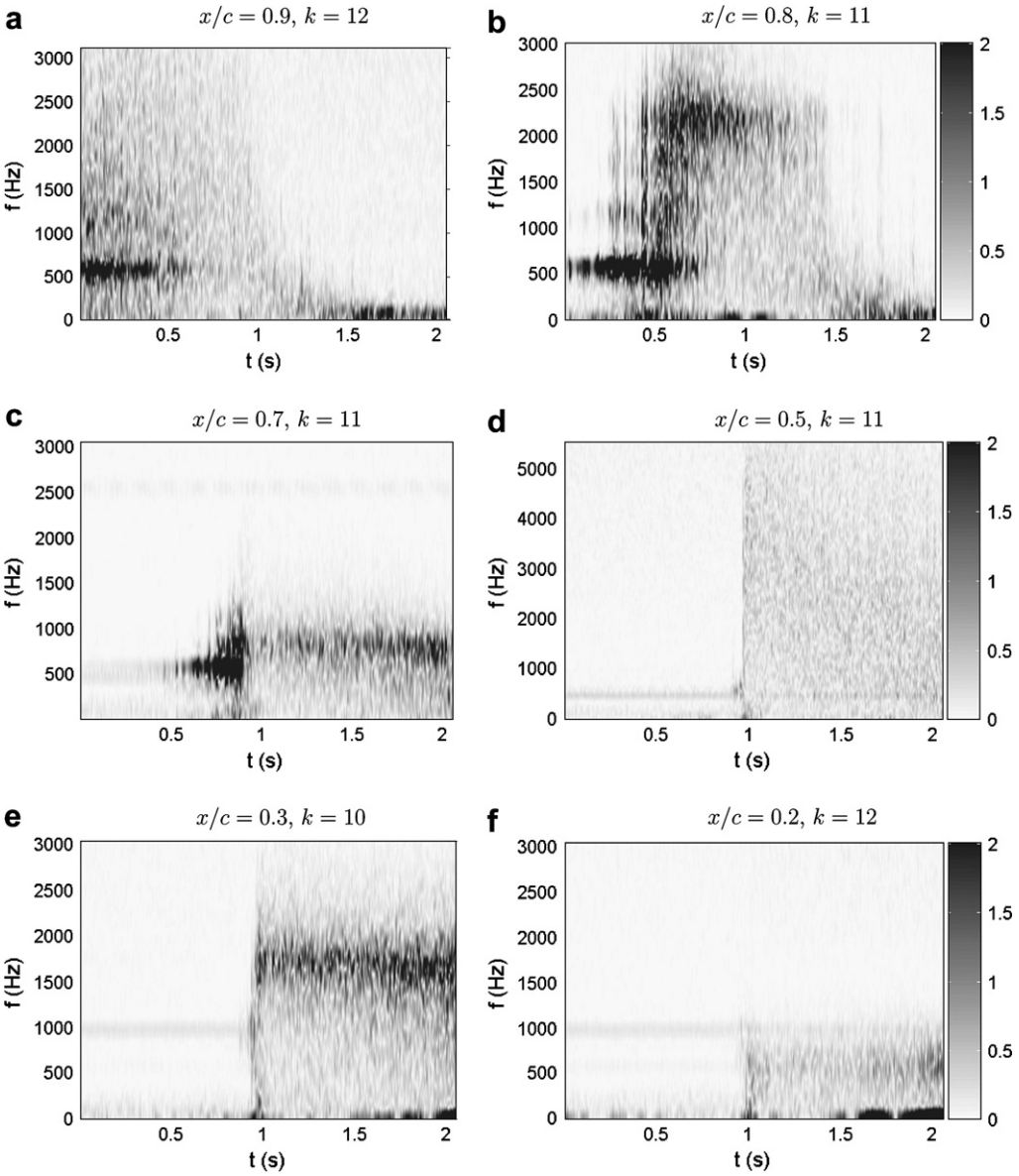

Fig. 14. Measurements, spectrograms from high frequency EMD fluctuation $\widetilde{C}_P(t)$ (Eq. (2)) as a function of time for various transducers along the suction side, $\dot{\alpha}^*=0.18$ and $\alpha=0$–12°, $Re=750\,000$.

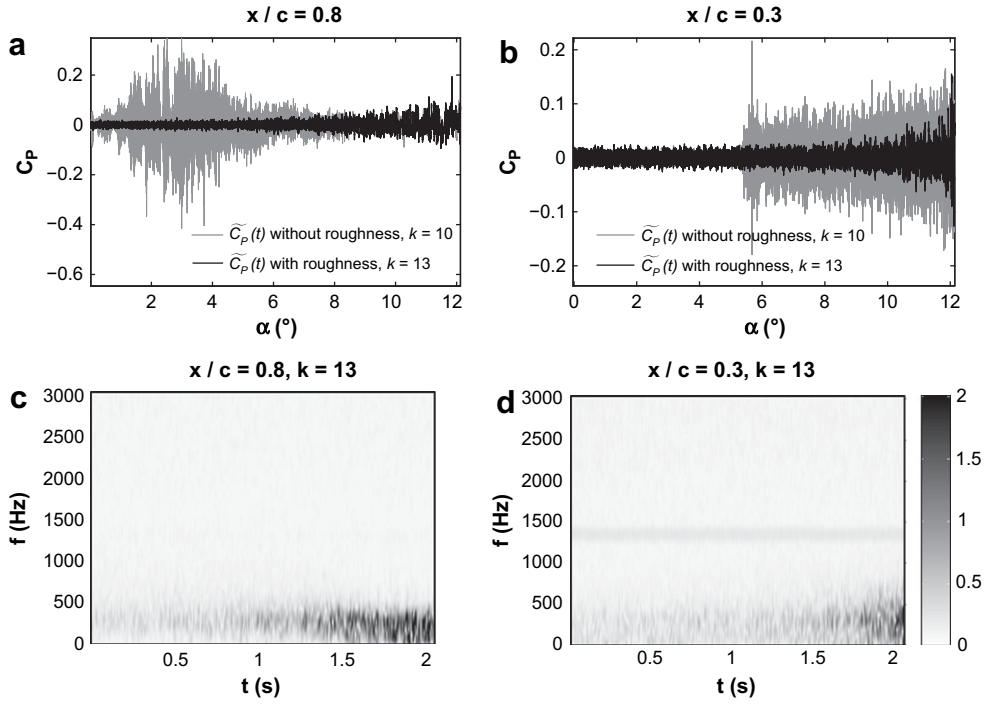

Fig. 15. Measurements, pressure fluctuations as function of the angle of incidence with and without roughness patch for $\dot{\alpha}^* = 0.18$, $\alpha = 0$–$12°$: (a) $x/c = 0.8$, (b) $x/c = 0.3$. Spectrograms from high frequency EMD pressure fluctuations $\widetilde{C}_P(t)$ (Eq. (2)) as function of time, experiments with roughness patch: (c) $x/c = 0.8$, (d) $x/c = 0.3$, $Re = 750\,000$.

a low amplitude frequency around 500 Hz whereas the transducer located downstream at $x/c = 0.5$ shows a broad frequency spectrum one can be the consequence of a fully turbulent flow.

The Strouhal number of vortex shedding $S_{t\theta}$ [10] is evaluated using the computed boundary layer momentum thickness $(\theta)_{sep}$ and the local upstream velocity $(v_e)_{sep}$ at separation and the experimental shedding frequencies. Before the transition passes near the leading edge, the LSB is located in a thick and developed boundary layer discretized into 20 layers. Computation gives mean values of $(\theta)_{sep} = 10.12 \times 10^{-5}$ m and $(v_e)_{sep} = 6.28$ m/s for α from 0° to 5°. This leads to $S_{t\theta} = 0.0088$ that can be compared to the $S_{t\theta} = 0.00686$ found by Pauley et al. in Ref. [10]. Computed boundary layer momentum thickness $(\theta)_{sep}$ and velocity $(v_e)_{sep}$ for α from 6° to 12° are respectively between $(\theta)_{sep} = 1.0 \times 10^{-5}$ m to 1.5×10^{-5} m and $(v_e)_{sep} = 7.135$ m/s to 8.135 m/s at separation point: this leads to $S_{t\theta} = 0.00238$–0.00313.

A roughness patch has been added on the leading edge in order to trigger the turbulence. Fig. 15 shows the comparison of pressure fluctuations with and without roughness for $x/c = 0.8$ and $x/c = 0.3$. The pressure fluctuations relied to LSB vortex shedding are not visible anymore on pressure signal with roughness. Fluctuations are weak for $\alpha = 0$–5° at $x/c = 0.8$ (trailing edge) as well as for $\alpha = 5$–12° at $x/c = 0.3$ (leading edge). Except for those zones, pressure fluctuations are the same. This clearly shows that the high pressure fluctuations observed earlier are relied to the presence of a LSB and to the transition to turbulence. The corresponding spectrograms of the signal obtained with roughness are shown in Fig. 15c and d and confirm this result: frequencies of $f = 550$ Hz and $f = 1700$ Hz have disappeared on both transducers. A low frequency around 200 Hz is observed and could be the consequence of trailing-edge separation. This frequency is not observed for the experiments without roughness patch because of the high amplitude frequencies induced by the vortex shedding of LSB; this has to be confirmed by future investigations.

4.2. Dynamic effects of pitching velocity on local pressure and boundary layer events

Fig. 16 is a comparison between numerical and experimental local wall pressures at $x/c = 0.3$ and $x/c = 0.8$ for pitching velocities ranging between $\dot{\alpha}^* = 0.618$ and $\dot{\alpha}^* = 1.89$. The increase of transient effects together with the pitching velocity does not affect the numerical prediction and the pressure variations due to laminar to turbulent transition is well predicted by computations in all cases. In particular, the pressure inflection resulting from the moves of the transition at the leading edge (at $\alpha = 5°$ for $\dot{\alpha}^* = 0.18$; see the previous section) can be seen for both computations and experiments. The transition is delayed when pitching velocity increases; as a consequence the transducer located at $x/c = 0.8$ in Fig. 16a shows a pressure inflection at $\alpha = 6°$ for $\dot{\alpha}^* = 0.618$ whereas it is delayed at $\alpha = 9°$ for $\dot{\alpha}^* = 1.89$ as shown in Fig. 16e.

Fig. 18a shows the transition and the trailing-edge separation and Fig. 18b shows the LSB length, obtained by computations for the considered pitching velocities. It illustrates that transition is delayed when pitching velocity increases. As a consequence, trailing-edge separation point is delayed and a higher lift coefficient before stall is induced. Pitching velocity does not have impact on the LSB size. Few variations appear when it forms but from $\alpha = 7°$ to stall, bubble lengths are the same. This correlation shows that high pitching velocities delay the separation induced transition phenomenon whereas boundary layer thickness and separation length are conserved. All these points have an impact on hydrodynamic loading of the foil.

Spectrograms of the experimental wall-pressure measurements are shown in Fig. 17. Frequencies observed on transducers at $x/c = 0.3$ and $x/c = 0.8$ are constant as functions of pitching velocity and are delayed in time compared to the lowest pitching velocity, which also means that the transition phenomenon is delayed as well.

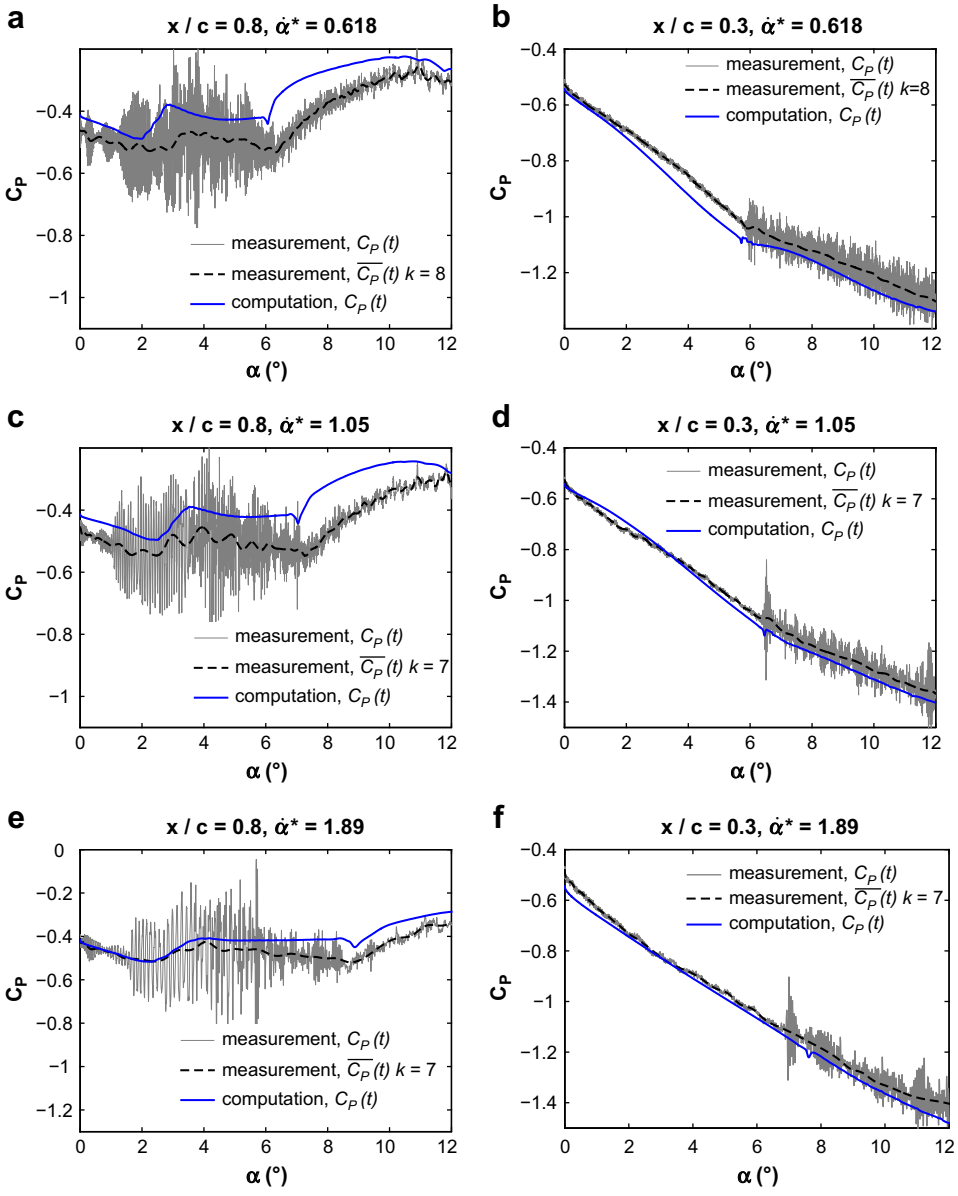

Fig. 16. Experimental and numerical pressure coefficient versus angle of incidence at $x/c = 0.8$ and $x/c = 0.3$ for various pitching velocities, $\alpha = 0$–$12°$. The dotted lines are the low frequency EMD pressure signals $\overline{C_P}(t)$ (Eq. (1)), $Re = 750\,000$.

4.3. Suction side loading analysis

Based on available experimental data, an analysis of suction side loading can be done by summing pressure coefficients on the suction side. The approximation can be written as:

$$C_l^+(t) = \sum_{i=2}^{10} C_p(x_i/c, t)\Delta(x_i/c) \tag{14}$$

where $C_p((x_i/c), t)$ is the pressure coefficient at location x_i/c and $\Delta(x_i/c)$ is the non-dimensional distance between two consecutive transducers. The procedure is applied to numerical data for comparison.

Fig. 19 shows the results obtained for the 4 pitching velocities. As shown, there is a good agreement between measurements and computations. The difference is very weak at the beginning of the pitching rotation and the inflection which appears at 5° for the lowest pitching velocity is accurately predicted by the transition model. It is delayed when pitching velocity increases and disappears even completely for the highest pitching velocity for both experimental and numerical approaches. High amplitude fluctuations at low frequency induced by leading-edge vortex shedding are over-predicted by computations but the phenomenon starts at an angle of incidence very close to measurement. This over-prediction can be explained by 3D effects which develop along the suction side and which are related to large structure of vortex shedding. The return to 0° shows hysteresis induced by a delay in the reattachment. Again, computations agree well to measurements even if the model tends to over predict the loading when the pitching velocity increases. Then it allows the authors to analyze the influence of pitching velocity on hydrodynamic coefficients obtained by computations.

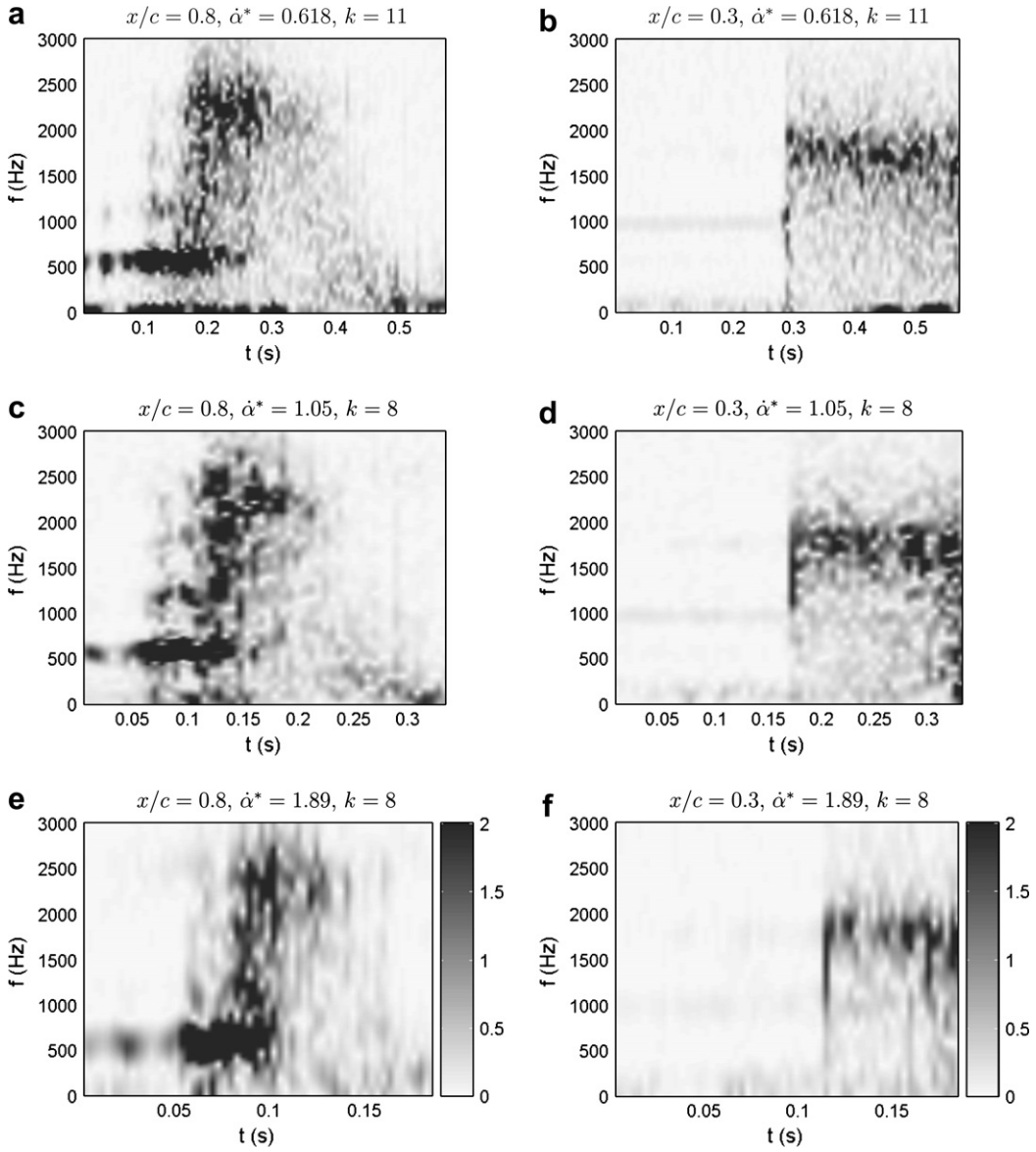

Fig. 17. Measurements, spectrograms from high frequency EMD pressure fluctuations $\widetilde{C}_P(t)$ (Eq. (2)) at $x/c = 0.8$ and $x/c = 0.3$ for various pitching velocities, $\alpha = 0$–12°, $Re = 750\,000$.

4.4. Dynamic effects of pitching velocity on hydrodynamic coefficients

Fig. 20 shows the numerical lift coefficient evolution as a function of the angle of incidence during pitching motion. This one is obtained by the integration of pressure over the whole foil surface. The laminar to turbulent transition appears to have a significant impact on lift when the pitching velocity is weak. An inflection is followed by a slope modification at 5° for $\dot{\alpha}^* = 0.18$ and 7° for $\dot{\alpha}^* = 1.05$ which tends to disappear for $\dot{\alpha}^* = 1.89$. So the highest pitching velocities tend to delay the transition of the boundary layer as well as it deletes the effect on hydrodynamic loading. This can be due to the diffusive time of the viscosity which becomes too high as compared to the pitching velocity. Then, we see that lift amplitude before stall is higher for high velocities. Stall appears at 13.3° for the lowest velocity and is delayed at 14.4° for the highest velocity. It is shown that high lift fluctuations induced by leading-edge vortex shedding appear for all pitching velocities, about three times for the lowest pitching velocity and only one time for the other ones. The flow reattachment is also delayed with high pitching velocities which induce an hysteresis effect. As a consequence, lift evolution is symmetric for $\dot{\alpha}^* = 0.18$ where the reattachment is located for $C_L = 1.33$ whereas $C_L = 0.16$ for $\dot{\alpha}^* = 1.89$.

Fig. 21 shows the drag coefficient (a) and the moment coefficient (b) versus the angle of incidence. Pitching velocity has some influence before the transition passes at the leading edge for both moment and drag coefficients. For the case $\dot{\alpha}^* = 0.18$ and $\alpha = 5^\circ$, $C_m = 0.087$ and $C_d = 0.0124$ whereas higher values are found for $\dot{\alpha}^* = 1.89$, $C_m = 0.107$ and $C_d = 0.0325$. It has been shown that the boundary layer is laminar from $\alpha = 0^\circ$ to 5°, so the increase can be attributed to inertia effects. Then, for the lower pitching velocity, the transition induces a slope modification of the drag curve due to the increase of wall shear stress because the boundary layer becomes turbulent. It also affects strongly the moment coefficient which decreases by a half. Again, the highest pitching velocity shows a disappearance of the transition effects. Drag coefficient is almost linear whereas a small inflection is found on the moment coefficient curve.

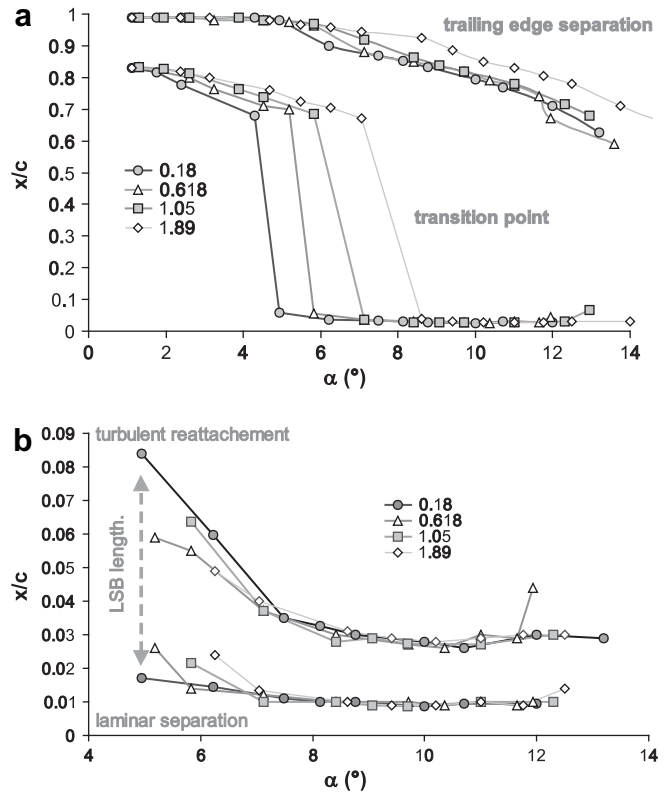

Fig. 18. Numerical prediction of: (a) boundary layer separation at leading edge and transition location on chord, (b) LSB length at leading edge on chord versus angle of incidence for various pitching velocities, $Re = 750\,000$.

5. Conclusion

The flow on the suction side of a NACA66 hydrofoil undergoing a transient pitching motion at a $Re = 0.75 \times 10^6$ has been carried out experimentally and numerically. Four reduced pitching velocities were studied from a low velocity $\dot{\alpha}^* = 0.18$ corresponding to a quasi-static case to a high velocity $\dot{\alpha}^* = 1.89$. The experiments were based on wall-pressure measurements using an array of wall-pressure transducers on the hydrofoil suction side. Computations were performed using a 2D RANS code including a laminar to turbulent transition model to take into account of the moderate Reynolds number. It was shown experimentally that during the foil rotation, the boundary layer experienced large modifications. Wall-pressure coefficients exhibited an inflection point at a given angle of incidence together with periodic wall-pressure fluctuations as a result of a laminar separation bubble (LSB) and boundary layer transition. The LSB and transition occurred near the trailing edge ($x/c = 0.8$) for low angles of incidence, moved progressively toward the leading edge as the angle of incidence increased and it was suddenly supplanted by a LSB and transition at the leading edge for a given angle of incidence depending on the pitching velocity ($\alpha = 5^\circ$ for the quasi-static case). Despite that some quantitative discrepancies existed, it was shown that boundary layer development including LSB and transition were quite well predicted numerically except for periodic wall-pressure fluctuations that were not captured by the RANS code. The influence of pitching velocity showed both experimentally and numerically that an increase of the pitching velocity delayed the boundary layer transition from about 5° for the lowest pitching velocity to about 8° for the highest pitching velocity. On the other hand, the LSB length and periodic pressure fluctuations were found to be constant versus pitching velocity. The effect of pitching velocities on boundary layer

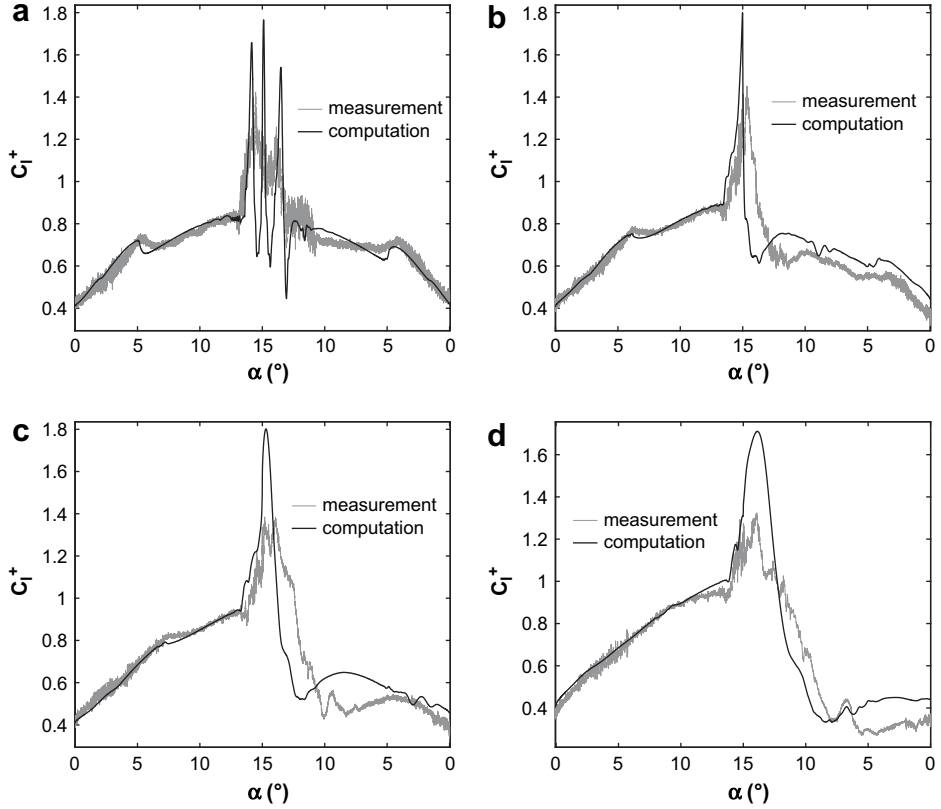

Fig. 19. Measurements versus computations, suction side loading versus angle of incidence during pitching motion: (a) $\dot{\alpha}^* = 0.18$, (b) $\dot{\alpha}^* = 0.618$, (c) $\dot{\alpha}^* = 1.05$ and (d) $\dot{\alpha}^* = 1.89$, $Re = 750\,000$.

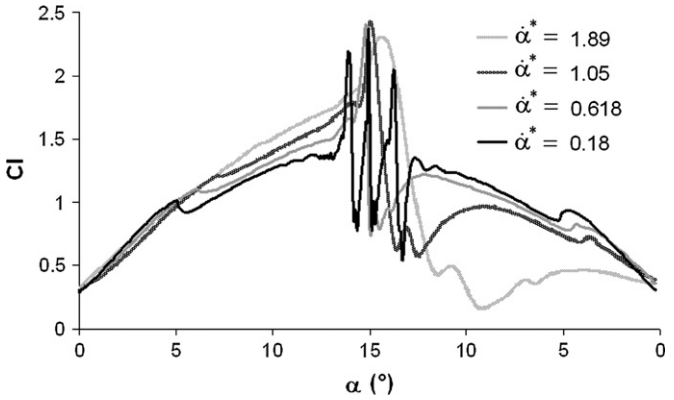

Fig. 20. Computations, lift coefficient as a function of the angle of incidence for $\alpha = 0$–15° followed by the return to 0°, for 4 pitching velocities $\dot{\alpha}^*$, $Re = 750\,000$.

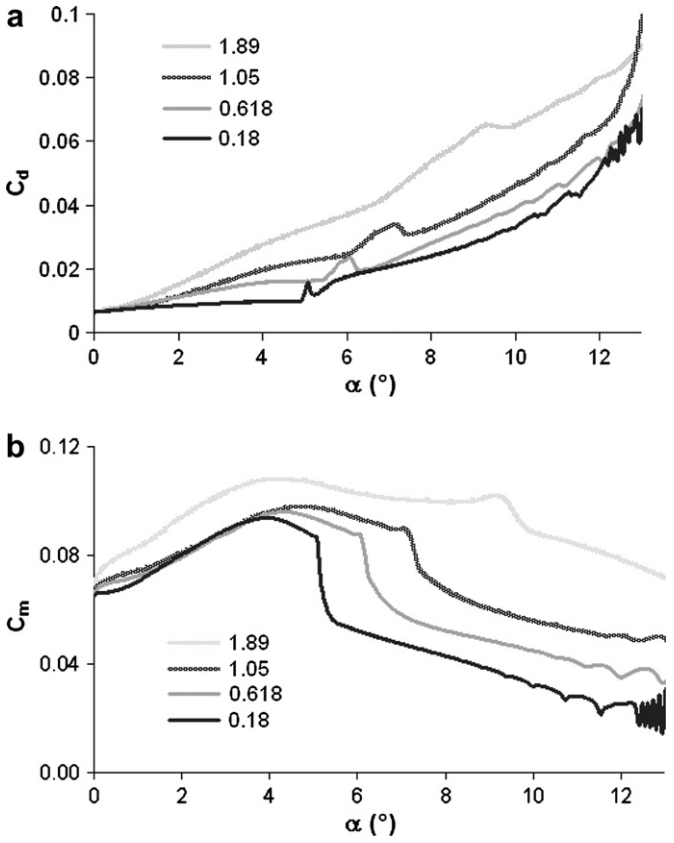

Fig. 21. Computations, (a) drag coefficient and (b) moment coefficient versus angle of incidence for 4 pitching velocities $\dot{\alpha}^*$, $Re = 750\,000$.

transition and hydrodynamic coefficients was highlighted. For the low pitching velocity, the transition induced a significant lift coefficient inflection at $\alpha = 5^\circ$. For higher pitching velocities the lift inflection is reduced and suppressed. In the latter case, the hydrofoil loading is strongly modified leading to higher lift values at stall together with a strong hysteresis effect during the downward motion.

Acknowledgment

The authors gratefully acknowledge the technical staff of IRENav for its contribution to the experimental set up.

References

[1] G.S. Triantafyllou, M.S. Triantafyllou, M. Grosenbaugh, Optimal thrust development in oscillating foils with application to fish propulsion, Journal of Fluids and Structures 7 (2) (1993) 205–224.
[2] G.R. Srinivasan, J.A. Ekaterinaris, W.J. McCroskey, Evaluation of Turbulence Models for Unsteady Flows of an Oscillating Airfoil, Pergamon; National Aeronautics and Space Administration; National Technical Information Service, Distributor, 1995.
[3] G.N. Barakos, Unsteady separated flows over manoeuvring lifting surfaces, Philosophical Transactions: Mathematical, Physical and Engineering Sciences 358 (1777) (2000) 3279–3291.
[4] H. Hamdani, M. Sun, Aerodynamic forces and flow structures of an airfoil in some unsteady motions at small Reynolds number, Acta Mechanica 145 (1) (2000) 173–187.
[5] T. Lee, P. Gerontakos, Investigation of flow over an oscillating airfoil, Journal of Fluid Mechanics 512 (2004) 313–341.
[6] I. Tani, Low-speed flows involving bubble separations, Progress in Aerospace Sciences 5 (1964) 70–103.
[7] M. Gaster, The Structure and Behaviour of Laminar Separation Bubbles, HMSO, 1969.
[8] M. Alam, N.D. Sandham, Direct numerical simulation of shortlaminar separation bubbles with turbulent reattachment, Journal of Fluid Mechanics 410 (2000) 1–28.
[9] A.E. Alving, H.H. Fernholz, Turbulence measurements around a mild separation bubble and downstream of reattachment, Journal of Fluid Mechanics Digital Archive 322 (2006) 297–328.
[10] L.L. Pauley, P. Moin, W.C. Reynolds, The structure of two-dimensional separation, Journal of Fluid Mechanics 220 (1990) 397–411.
[11] Z. Yang, P.R. Voke, Large-eddy simulation of boundary-layer separation and transition at a change of surface curvature, Journal of Fluid Mechanics 439 (2001) 305–333.
[12] M. Marquillie, U. Ehrenstein, On the onset of nonlinear oscillations in a separating boundary-layer flow, Journal of Fluid Mechanics 490 (2003) 169–188.
[13] U. Rist, U. Maucher, Investigations of time-growing instabilities in laminar separation bubbles, European Journal of Mechanics/B Fluids 21 (5) (2002) 495–509.
[14] L.E. Jones, R.D. Sandberg, N.D. Sandham, Direct numerical simulations of forced and unforced separation bubbles on an airfoil at incidence, Journal of Fluid Mechanics 602 (2008) 175.
[15] M.J. Smith, T.C. Wong, M. Potsdam, J. Baeder, S. Phanse, Evaluation of CFD to determine two-dimensional airfoil characteristics for rotorcraft applications, in: American Helicopter Society 60th Annual Forum, Baltimore, MD, June 7–10, 2004.
[16] A. Shelton, J. Abras, B. Hathaway, M. Sanchez-Rocha, M.J. Smith, S. Menon, An investigation of the numerical prediction of static and dynamic stall, Proceedings of the 61 American Helicopter Society Annual Forum, Grapevine 10 (10) (2005) 6.
[17] J.B. Leroux, O. Coutier-Delgosha, J.A. Astolfi, A joint experimental and numerical study of mechanisms associated to instability of partial cavitation on two-dimensional hydrofoil, Physics of Fluids 17 (2005) 052101.
[18] J. Leroux, J. Astolfi, J. Billard, An experimental study of unsteady partial cavitation, Journal of Fluids Engineering (Transactions of the ASME) 126 (1) (2004) 94–101.
[19] N.E. Huang, Z. Shen, S.R. Long, M.C. Wu, H.H. Shih, Q. Zheng, N.C. Yen, C.C. Tung, H.H. Lui, The empirical mode decomposition and the Hilbert spectrum for nonlinear and non-stationary time series analysis, Proceedings of the Royal Society of London A 454 (1998) 903–995.
[20] S. Benramdane, J.C. Cexus, J.A. Astolfi, A.O. Boudraa, Time–frequency analysis of pressure fluctuations on a hydrofoil undergoing a transient pitching motion using Huang-Hilbert and Huang-Teager transforms, in: ASME PVP-2007/CREEP-8 Conference, July 22–26, San Antonio, Texas, USA, 2007.
[21] A. Ducoin, S. Benramdane, J.A. Astolfi, F. Deniset, Etude expérimentale et numérique du champ de pression pariétale sur corps portant en mouvement forcé, in: 18eme Congres Français de Mécanique, 2007.
[22] S. Benramdane, J.A. Astolfi, J.C. Cexus, A. Boudraa, Etude expérimentale du champ de pression pariétale sur un hydrofoil en mouvement forcé transitoire, in: Proceedings des 11emes journées de l'hydrodynamique, 3–5 avril, Brest, France, 2005.
[23] T. Barth, D. Jespersen, The design and application of upwind schemes on unstructured meshes, in: AIAA, Aerospace Sciences Meeting, 27th, Reno, NV, 1989.
[24] I. Demirdzic, M. Peric, Space conservation law in finite volume calculations of fluid flow, International Journal for Numerical Methods in Fluids 8 (1988) 1037–1050.
[25] M. Behr, T. Tezduyar, The shear-slip mesh update method, Computer Methods in Applied Mechanics and Engineering 174 (3–4) (1999) 261–274.
[26] M. Behr, T. Tezduyar, Shear-slip mesh update in 3D computation of complex flow problems with rotating mechanical components, Computer Methods in Applied Mechanics and Engineering 190 (24–25) (2001) 3189–3200.
[27] G. Markou, Z. Mouroutis, D. Charmpis, M. Papadrakakis, The ortho-semi-torsional (OST) spring analogy method for 3D mesh moving boundary problems, Computer Methods in Applied Mechanics and Engineering 196 (4–6) (2007) 747–765.

[28] F.R. Menter, Improved two-equation *k*-turbulence models for aerodynamic flows, NASA Technical Memorandum 103975 (1993) 34.
[29] F.R. Menter, M. Kuntz, R. Langtry, Ten years of industrial experience with the SST turbulence model, Turbulence, Heat and Mass Transfer 4 (2003) 625–632.
[30] W. Haase, B. Aupoix, U. Bunge, D. Schwamborn, FLOMANIA—A European Initiative on Flow Physics Modelling, Springer, Berlin, 2006, ISBN 3-540-28786-8.
[31] B.J. Abu-Ghannam, R. Shaw, Natural transition of boundary layers—the effects of turbulence, pressure gradient, and flow history, Journal of Mechanical Engineering Science 22 (1980) 213–228.
[32] J. Steelant, E. Dick, Modelling of bypass transition with conditioned intermittency transport equation, International Journal for Numerical Methods in Fluids 23 (1996) 193–220.
[33] F.R. Menter, R. Langtry, S. Völker, Transition modelling for general purpose CFD codes, Flow, Turbulence and Combustion 77 (1) (2006) 277–303.
[34] M. Dular, R. Bachert, B. Stoffel, B. Širok, Influence of the velocity distribution at the inlet boundary on the CFD prediction of local velocity and pressure fields around a hydrofoil, Experimental Thermal and Fluid Science 32 (2007) 882–891.
[35] N. Maman, C. Farhat, Matching fluid and structure meshes for aeroelastic computations: a parallel approach, Computers and Structures 54 (4) (1995) 779–785.
[36] C. Farhat, M. Lesoinne, P. Le Tallec, Load and motion transfer algorithms for fluid/structure interaction problems with non-matching discrete interfaces: momentum and energy conservation, optimal discretization and application to aeroelasticity, Computer Methods in Applied Mechanics and Engineering 157 (1–2) (1998) 95–114.
[37] T.E. Tezduyar, S. Sathe, R. Keedy, K. Stein, Space–time finite element techniques for computation of fluid–structure interactions, Computer Methods in Applied Mechanics and Engineering 195 (17–18) (2006) 2002–2027.
[38] C.P. Haggmark, A.A. Bakchinov, P.H. Alfredsson, Experiments on a two-dimensional laminar separation bubble, Philosophical Transactions: Mathematical, Physical & Engineering Sciences 358 (1777) (2000) 3193–3205.